



Article

# Automated Cloud Shadow Detection from Satellite Orthoimages with Uncorrected Cloud Relief Displacements

Hyeonggyu Kim, Wansang Yoon and Taejung Kim \*

Department of Geoinformatic Engineering, Inha University, Incheon 22212, Republic of Korea; rstarshine@3dlabs.co.kr (H.K.); wsyoon@3dlabs.co.kr (W.Y.)

\* Correspondence: tezid@inha.ac.kr

Abstract: Clouds and their shadows significantly affect satellite imagery, resulting in a loss of radiometric information in the shadowed areas. This loss reduces the accuracy of land cover classification and object detection. Among various cloud shadow detection methods, the geometric-based method relies on the geometry of the sun and sensor to provide consistent results across diverse environments, ensuring better interpretability and reliability. It is well known that the direction of shadows in raw satellite images depends on the sun's illumination and sensor viewing direction. Orthoimages are typically corrected for relief displacements caused by oblique sensor viewing, aligning the shadow direction with the sun. However, previous studies lacked an explicit experimental verification of this alignment, particularly for cloud shadows. We observed that this implication may not be realized for cloud shadows, primarily due to the unknown height of clouds. To verify this, we used Rapideye orthoimages acquired in various viewing azimuth and zenith angles and conducted experiments under two different cases: the first where the cloud shadow direction was estimated based only on the sun's illumination, and the second where both the sun's illumination and the sensor's viewing direction were considered. Building on this, we propose an automated approach for cloud shadow detection. Our experiments demonstrated that the second case, which incorporates the sensor's geometry, calculates a more accurate cloud shadow direction compared to the true angle. Although the angles in nadir images were similar, the second case in high-oblique images showed a difference of less than  $4.0^{\circ}$  from the true angle, whereas the first case exhibited a much larger difference, up to 21.3°. The accuracy results revealed that shadow detection using the angle from the second case improved the average F1 score by 0.17 and increased the average detection rate by 7.7% compared to the first case. This result confirms that, even if the relief displacement of clouds is not corrected in the orthoimages, the proposed method allows for more accurate cloud shadow detection. Our main contributions are in providing quantitative evidence through experiments for the application of sensor geometry and establishing a solid foundation for handling complex scenarios. This approach has the potential to extend to the detection of shadows in high-resolution satellite imagery or UAV images, as well as objects like high-rise buildings. Future research will focus on this.

**Keywords:** cloud shadow detection; shadow direction; cloud relief displacement; orthoimage; directional vector of cloud shadow



Citation: Kim, H.; Yoon, W.; Kim, T. Automated Cloud Shadow Detection from Satellite Orthoimages with Uncorrected Cloud Relief Displacements. *Remote Sens.* **2024**, *16*, 3950. https://doi.org/10.3390/rs16213950

Academic Editor: Filomena Romano

Received: 3 August 2024 Revised: 19 October 2024 Accepted: 21 October 2024 Published: 23 October 2024



Copyright: © 2024 by the authors. Licensee MDPI, Basel, Switzerland. This article is an open access article distributed under the terms and conditions of the Creative Commons Attribution (CC BY) license (https://creativecommons.org/licenses/by/4.0/).

# 1. Introduction

The utility of optical satellites is increasing due to their ability to periodically observe extensive regions and to enable effective Earth observation missions [1]. However, despite these significant advantages, satellite imagery, particularly in the field of remote sensing, could present various challenges. One such challenge encountered in this field is shadows [2]. Shadows could be caused by different sources, such as buildings, clouds, and terrain. Shadows from these objects could lead to misleading outcomes like classification or object detection because the presence of shadows leads to a significant loss of radiometric information in the shadowed areas [2,3]. This vulnerability also affects the

Remote Sens. 2024, 16, 3950 2 of 22

unmanned aerial vehicle (UAV) remote sensing [4,5]. Liu et al. [5] reported that shadows in UAV images significantly affect subsequent image processing tasks, including image interpretation, image matching, feature extraction, land cover classification, and digital photogrammetry in UAV remote sensing. Given the significant impact shadows could have on the accuracy and reliability of satellite imagery, many researchers perceive shadows as noise and targets for removal or correction in detection operations [6]. Building upon the general challenges posed by shadows, cloud shadows also present significant issues in optical satellite imagery. Due to the annual average cloud cover of 66% [7], a significant amount of information is lost as a result of clouds and the corresponding cloud shadows. As noted above, the presence of clouds and cloud shadows in optical satellite images could interfere with ground observations [8–10]. Therefore, detecting clouds and cloud shadows is crucial for ensuring the reliability of satellite imagery [11].

In recent years, many researchers have developed cloud shadow detection using deep learning methods. Zhang et al. [12] proposed the CRSNet model, a deep learning model based on ResNet-18, designed to enhance cloud and cloud shadow segmentation. Tan et al. [13] proposed the Swin-UNet model, which improves cloud and cloud shadow detection in GF-1 satellite images. While deep learning models achieve high accuracy in cloud and shadow detection, they are heavily reliant on large, labeled datasets. The geometric-based method uses physical principles, such as the position of the sun and the viewing angles of the sensor, to provide reliable results in cloud and cloud shadow detection. These methods do not require large-scale training datasets like deep learning. Moreover, since they follow physical rules, geometric methods can deliver consistent performance across various environments and offer easier interpretability of results.

Zhu and Woodcock [14] conducted cloud and cloud shadow detection for the Landsat and Sentinel-2 satellites. Within the scope of cloud shadows, this method involves estimating the projected location of cloud shadows from cloud masks detected a priori by considering the solar and satellite azimuth and zenith angles. Foga et al. [15] reported that this method is well performed and tested by the United States Geological Survey (USGS). In high-resolution satellite imagery, Le Hégarat-Mascle and André [16] and Fisher [17] developed a cloud shadow detection method focusing on the geometric relationship between clouds and their shadows for SPOT satellite images. Similarly, Zhong et al. [18] also developed a cloud shadow detection method based on the geometric relationships for Chinese satellite images.

As shown in the above developments, it is well known that the direction of a shadow in raw satellite images depends on the direction of sun illumination and sensor viewing direction. It is also well known that orthorectified images remove relief displacements due to the oblique sensor viewing direction. This implies that the direction of a shadow and the direction of sun illumination should coincide in orthorectified images. However, we observed that this implication may not be realized for objects such as clouds and cloud shadows. The reason is that the height of clouds is not considered during the orthorectification process, leading to relief displacement concerning cloud height in orthoimages. This phenomenon was also mentioned in the study by Pailot-Bonnétat et al. [19], however, without explicit experiments. Moreover, it is important to note that the influence of the relief displacement of clouds in orthoimages becomes more pronounced as the image resolution increases. For lower-resolution imagery, such as Landsat (30 m/pixel), the relief displacement may only occur at sub-pixel levels, making it relatively less impactful. However, in high-resolution imagery, this shift can be more dramatic, directly affecting the accuracy of shadow detection.

In this paper, we highlight the necessity of the direction of sensor viewing as well as that of sun illumination for determining the direction of the shadow of objects with uncorrected relief displacements, such as clouds. To address the lack of explicit experimental verification in previous studies, including that of Pailot-Bonnétat et al. [19], we conducted experiments to confirm that the relief displacement of clouds still exists in orthoimages and to point out the importance of considering sensor geometry for cloud shadow detection

Remote Sens. 2024, 16, 3950 3 of 22

from orthoimages. Building upon this, we propose an automated approach for cloud shadow detection that involves shifting a bounding box around each cloud one pixel at a time, performing spectral testing. These experiments provide empirical evidence supporting the importance of sensor geometry in cloud shadow detection from orthoimages. The key contributions of this paper are as follows:

- By applying both solar and sensor geometry, the difference from a value of the true angle
  was significantly reduced compared to using solar geometry alone, leading to more precise
  cloud shadow detection in orthoimages, particularly in high-oblique imagery.
- It laid the foundation for further improvement and application in complex scenarios involving the interaction between sun and sensor geometry through experiments.
- This approach showed potential for extending its use to high-resolution satellite imagery and UAV imagery, especially for detecting shadows of objects with uncorrected relief displacements, such as high-rise buildings.

### 2. Methods

## 2.1. Summary of Cloud Shadow Detection Process

The cloud shadow detection method proposed in this study consists of three main steps, the data preprocessing, estimation of the search range for cloud shadow detection, and detection of cloud shadows, as illustrated in Figure 1. In the preprocessing step, the pixel values of a satellite image are converted to Top-of-Atmosphere (TOA) values, and cloud pixels are detected by the OCM (Object-oriented Cloud and Cloud shadow Matching) method previously researched by Zhong et al. [18]. In the search range estimation step, metadata at the time of satellite image acquisition, including the satellite and solar zenith and azimuth angles, are used to calculate the direction vector from clouds to cloud shadows. Subsequently, the search range where cloud shadows may be projected was calculated by presumed minimum and maximum cloud heights. In the cloud shadow detection step, the process involves shifting cloud pixels from the minimum to maximum range incrementally along the direction of cloud shadows. Cloud shadows are then detected by selecting the value that shows the best spectral characteristics of cloud shadows.

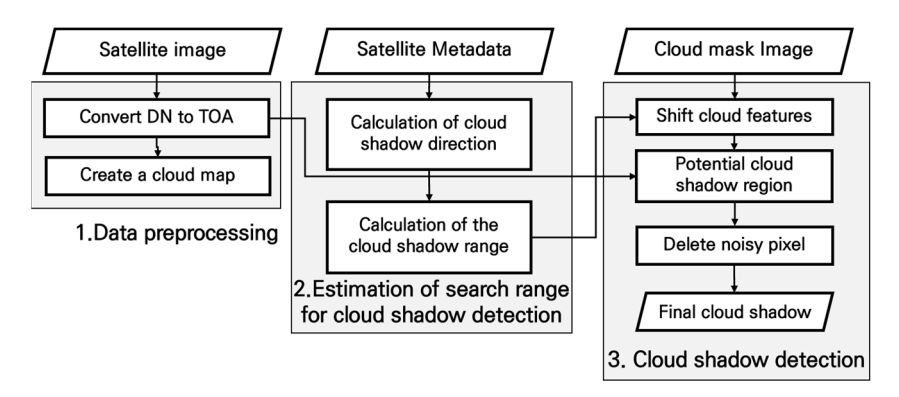


Figure 1. A workflow of the cloud shadow detection method.

# 2.2. Data Preprocessing

The pixel values (Digital Number, DN) in a satellite image contain distortions due to variations in the solar angle resulting from temporal differences, changes in the distance between the sun and Earth, and spectral differences [20]. Distortions result in variations in pixel values between images, making it challenging to accurately determine the physical quantities of the surface [21]. Therefore, a process is necessary to convert pixel values into reflectance values corrected for distortions. This study employed Equations (1) and (2) to convert pixel values into Top-of-Atmospheric reflectance (TOA reflectance) values from the Product Specification provided by Planet Labs [22]. In Equation (1), RAD(i) represents the radiance of the i-th band, where i denotes the number of bands, and ScaleFactor denotes the coefficient for radiance conversion. In Equation (2),  $REF_{TOA}(i)$  represents the Top-of-

Remote Sens. 2024, 16, 3950 4 of 22

Atmospheric reflectance of the i-th band, SunDist is the distance between the Earth and the sun at the time of image acquisition, EAI(i) denotes Exo-Atmospheric Irradiance, and SolarZenith represents the solar zenith angle. The cloud map is generated using a cloud map with low confidence (CML) of the OCM method. The CML represents the operation of loosening the thresholds of the VNIR bands to sufficiently detect clouds [18].

$$RAD(i) = DN(i) \times ScaleFactor,$$
 (1)

$$REF_{TOA}(i) = \frac{RAD(i) \times \pi \times SunDist}{EAI(i) \times Cos(SolarZenith)},$$
(2)

## 2.3. Estimation of Search Range for Cloud Shadow Detection

# 2.3.1. Calculation of Cloud Shadow Direction

The geometric principle behind shadow formation is that sunlight is obstructed by objects, resulting in the casting of shadows opposite to the solar direction. Shadows can be detected by utilizing the solar azimuth angle and the height of the object. However, as mentioned in the introduction, considering the geometry of the sensor is essential for cloud shadow detection. This is illustrated in Figures 2–4. Figure 2a illustrates the projected locations of cloud shadows based on the height of the clouds.  $C_0$  represents the true ground location of the clouds.  $C_1$  and  $C_2$  represent cloud locations at different heights,  $\Delta h_1$  and  $\Delta h_2$ .  $CS_1$  and  $CS_2$  denote the projected cloud shadows from  $C_1$  and  $C_2$  due to the oblique sun direction.

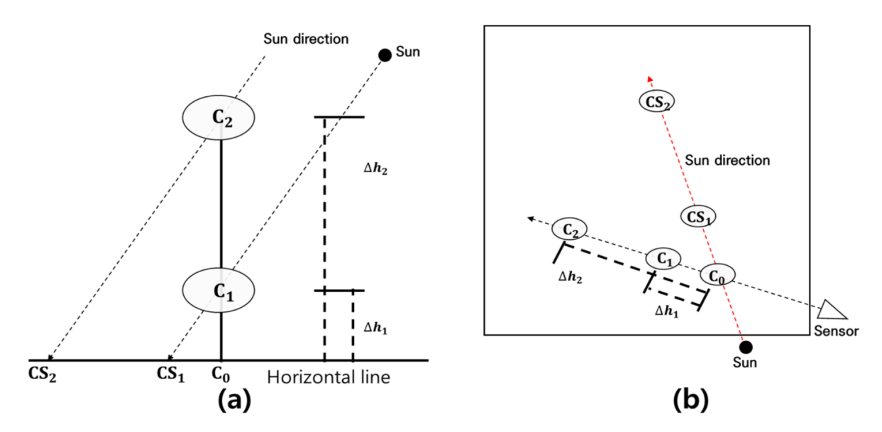


**Figure 2.** Illustrations of the location where cloud shadows are projected: (a) a case where cloud shadows are projected based on the height of the clouds; (b) the position of clouds and cloud shadows depicted in the image.

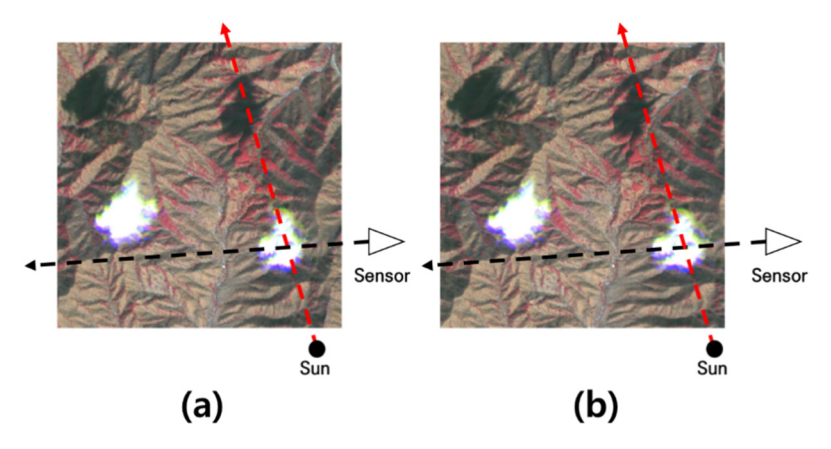


**Figure 3.** An example of the positions of clouds and cloud shadows in satellite images: (a) before orthorectification; (b) after orthorectification.

Remote Sens. 2024, 16, 3950 5 of 22

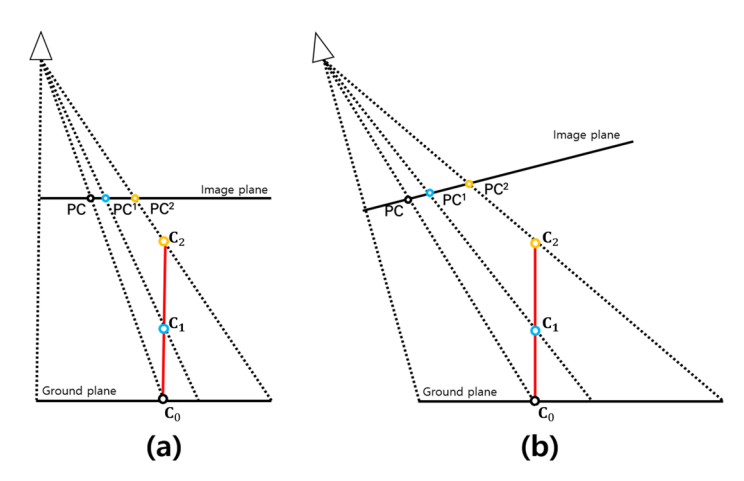


**Figure 4.** Illustrations depicting the cloud relief displacement: (a) a case of a vertical image; (b) a case of a high-oblique image.

Figure 2b illustrates the positions of clouds and cloud shadows projected in an orthoimage. If orthorectification is performed ideally by considering the height of clouds, all clouds would be positioned at  $C_0$  in Figure 2b. The cloud shadows for clouds with various heights would be projected along the line from the sun to  $C_0$ . However, in reality, the displacement due to cloud height will not be corrected during the orthorectification process. As a result, clouds depicted in the orthoimage are positioned along the line from the sensor to  $C_0$  on  $C_1$  to  $C_2$  according to their heights. With an increase in cloud height, relief displacement occurs in the orthoimages, posing a challenge in estimating cloud shadow positions solely based on the geometry of the sun [19].

Figure 3 illustrates clouds and their shadows in the original images before orthorectification (a) and in the orthoimage (b). The cloud shadow pixels in (b) have been orthorectified based on the height information from the corresponding surface heights. As a result, it is challenging to discern significant differences between the cloud and cloud shadow positions in (a) and (b). This indicates that the cloud relief displacement in the orthoimages has not been effectively corrected.

Figure 4 illustrates the cloud relief displacement caused by the satellite's viewing angle. Figure 4a,b illustrate the positions of cloud relief displacement in vertical and oblique images, respectively. Here,  $C_0$  represents the ground point directly beneath the cloud, and  $C_1$  and  $C_2$  indicate clouds at different heights; PC, PC<sup>1</sup>, and PC<sup>2</sup> represent the positions of the projected ground point below the clouds and the positions of the clouds based on their heights. As the satellite captures images at a more oblique angle, PC<sup>2</sup> in (b) exhibits a more pronounced relief displacement compared to PC<sup>2</sup> in (a). In summary, relief displacement in cloud height persists in orthoimages. As the satellite captures images at higher angles, the variation in cloud height becomes more pronounced. Therefore, it is crucial to consider the satellite's azimuth and zenith angle, which allows for the incorporation of cloud height variations.

To detect clouds that still exhibit relief displacement in orthoimages, it is necessary to determine the direction from clouds to their shadows. The calculation method for the cloud-to-shadow unit vector ( $\hat{C}$ ) is illustrated in Figure 5. Since the relief displacement of clouds is not corrected in orthoimages, the clouds are projected onto the position of the projected cloud in Figure 5. When applying the solar unit vector ( $\hat{S}$ ), the projected cloud does not align with the direction of the cloud shadow. Therefore, it is necessary to consider the sensor unit vector ( $\hat{V}$ ). Both unit vectors ( $\hat{S}$  and  $\hat{V}$ ) could be calculated using the metadata at the time of image acquisition.  $\hat{C}$  can be obtained through the difference operation of  $\hat{S}$  and  $\hat{V}$ , as shown in Equation (3). The difference operation of  $\hat{S}$  and  $\hat{V}$  is computed as shown in Equation (5), and the cloud shadow azimuth ( $\varphi_c$ ) calculated from this could be used to derive  $\hat{C}$ , as in Equation (4). In Equation (5),  $\theta_S$ ,  $\theta_S$ ,  $\theta_V$ , and  $\phi_V$ 

Remote Sens. 2024, 16, 3950 6 of 22

represent, respectively, the solar zenith and azimuth angles and the sensor zenith and azimuth angles.

$$\hat{C} = \hat{S} - \hat{V},\tag{3}$$

$$\hat{C} = \begin{bmatrix} \cos \varphi_c & \sin \varphi_c & 0 \end{bmatrix}^T, \tag{4}$$

$$\varphi_c = \pi + \tan^{-1} \left( \frac{(\tan(\theta_S) \times \sin(\varphi_S)) - (\tan(\theta_V) \times \sin(\varphi_V))}{(\tan(\theta_S) \times \cos(\varphi_S)) - (\tan(\theta_V) \times \cos(\varphi_V))} \right), \tag{5}$$

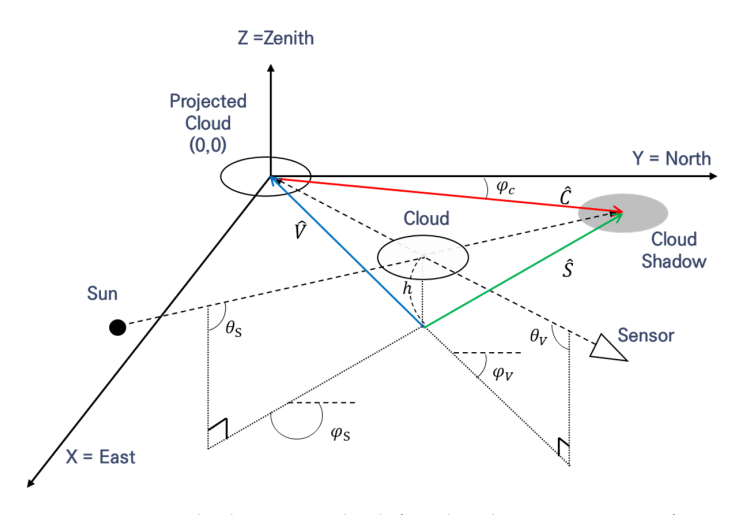


**Figure 5.** A calculation method for the direction vector from a cloud to cloud shadow in a 3-dimensional coordinate system.

# 2.3.2. Calculation of Cloud Shadow Range

Once the cloud-to-shadow direction is determined, cloud shadow locations can be determined using the height of clouds [18]. However, in optical satellites, it is not possible to determine the height of the cloud. It is necessary to make assumptions about the minimum and maximum heights of the cloud to estimate the search range for cloud shadow detection. In mid-latitude regions of the Northern Hemisphere, excluding tropical areas, the maximum height of clouds is known to be 12 km [18,23]. The minimum height varies depending on the research; however, based on previous studies [24], we assumed a minimum cloud height of 200 m, as illustrated in Figure 6. The minimum–maximum search range  $(D_{(m)})$  for cloud shadows is calculated using the minimum–maximum height of clouds  $(h_{min})$  and  $h_{max}$  and the cloud-to-cloud shadow unit vector  $(\hat{C})$ , as shown in Equation (6).

$$D_{(m)} = h \times ||\hat{C}||, \tag{6}$$

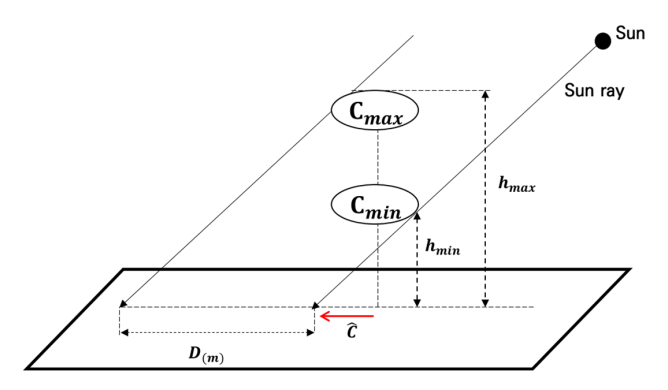


Figure 6. Explanation for search range of cloud shadow based on cloud height.

Remote Sens. **2024**, 16, 3950 7 of 22

#### 2.4. Cloud Shadow Detection

The proposed cloud shadow detection method in this study involves shifting the clouds using the search range for cloud shadows and the cloud shadow direction angle. Subsequently, a near-infrared band-based statistical analysis is conducted to identify the point with the minimum value, indicating the detection of cloud shadows.

Clouds have varying heights for each object; hence, cloud shadow detection needs to be performed for each cloud object. In this study, we employ the outline information of clouds within the cloud mask to individually extract cloud objects. The clouds extracted for each object are shifted based on the Ground Sample Distance (GSD) in the cloud shadow direction angle, ranging from the minimum to the maximum detectable distance. To calculate the shifted position of clouds, the ground coordinates of the shifted clouds are computed using Equations (7) and (8) as shown in Figure 7. These ground coordinates are then transformed into image coordinates.

$$\begin{bmatrix} Xcloud_{geo} \\ Ycloud_{geo} \end{bmatrix} = \begin{bmatrix} X\_Img_{geo} + (GSD_x \times Boundary_{ULx}) + D_{(m)} \times Cos(\varphi_c) \\ Y\_Img_{geo} + \left(GSD_y \times Boundary_{ULy}\right) + D_{(m)} \times Sin(\varphi_c) \end{bmatrix}, \tag{7}$$

$$\begin{bmatrix}
Xcloud_{Img} \\
Ycloud_{Img}
\end{bmatrix} = \begin{bmatrix}
\frac{(Xcloud_{geo} - X_{Img_{geo}})}{GSD_x} & \frac{(Ycloud_{geo} - Y_{Img_{geo}})}{GSD_y}
\end{bmatrix}^T,$$
(8)

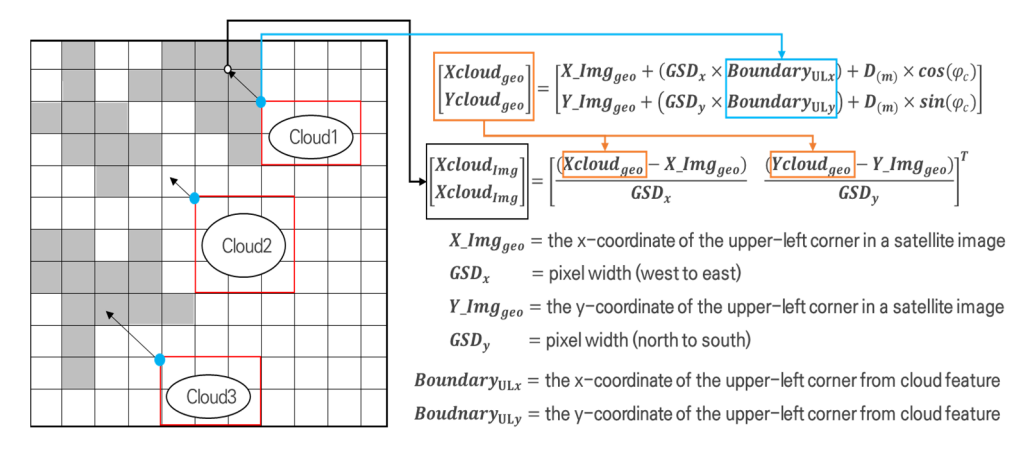


Figure 7. Calculation method for cloud object movement in image coordinates using ground coordinate.

Due to the unavailability of the true cloud height or the true distance of shadow projection for each cloud object, it is essential to incorporate a measure considering the spectral characteristics of cloud shadows. The formulation of the measure is as follows, with the spectral thresholds referencing and redesigning the approach outlined in the study by Zhong et al. [18]: First, cloud shadows typically exhibit low reflectance in the near-infrared (NIR) band. This is because shadowed areas appear darker in the NIR band due to reduced diffuse radiation at longer wavelengths (e.g., NIR band), as atmospheric scattering is stronger at shorter wavelengths (e.g., visible band) [16,25,26]. Second, to identify points with low reflectance values, it is imperative to exclude cloud areas with the cloud mask from operation. Third, the areas that are the most affected by the shadow correspond to areas where the sum of NIR reflectance within the shifted cloud mask is at its minimum. Accordingly, we define the measure in Equation (9), and its explanation is provided below. x represents pixels; A represents the region of a shifted cloud object; B represents the cloud mask map; h(x) represents the statistics of the NIR band within the shifted cloud mask, as defined in Equation (10); f(x) represents the region of cloud objects satisfying the condition; and g(x) represents the objective function to satisfy the minimum value among the cloud object regions that meet the condition. In Equation (10),  $\mu_{NIR}$  and

Remote Sens. 2024, 16, 3950 8 of 22

 $\sigma_{NIR}$  represent the mean and standard deviation of the NIR band, respectively.  $\alpha$  denotes the Z-score, and a value of 1.96 was applied for  $\alpha$ .

$$g(x) = \begin{cases} if \ x \in A \setminus B \ and \ h(x) < 0.17 \ and \ D_{(m)} \leq D_{max} \ then \ f(x), \\ if \ x \in A \setminus B \ and \ h(x) \geq 0.17 \ and \ D_{(m)} > D_{max} \ then \ \neq Cloud \ shadow, \end{cases}$$
 (9) 
$$otherwise \qquad then \ next \ loop,$$

$$h(x) = (\mu_{NIR} + \alpha \times \sigma_{NIR}), \tag{10}$$

Potential Cloud Shadow Region(PCSR) = 
$$argmin[f(x)],$$
 (11)

$$\textit{Potential Cloud Shadow} = \left(\textit{NIR}_{TOA} < 0.17 \ \textit{and} \ \frac{\textit{NIR}_{TOA}}{\textit{RED}_{TOA}} > 1.0\right) \in \textit{PCSR}, \tag{12}$$

We detect cloud shadows in the following procedures. If the distance of the shifted cloud object is less than the maximum detectable distance  $(D_{max})$ , the iterative process is repeated by moving one pixel along the cloud shadow direction. Through iterative operations, the region with the lowest statistics in the near-infrared band is identified and confirmed as the cloud shadow region. This region is formally defined as the Potential Cloud Shadow Region (PCSR), as described by Equation (11). Within the confirmed area, we detect Potential Cloud Shadow (PCS) pixels using Equation (12). In the paper by Zhong et al. [18], it was stated that the NIR-RED ratio is less than 1. However, this did not apply to pixels where forests and shadows were mixed, as illustrated in Figure 8a. This is because when cloud shadows are projected onto forests, the NIR values from vegetation mix with those of the shadows, resulting in higher NIR readings than typical shadow areas. In Figure 8b, the middle image shows the NIR TOA values when applying a threshold of 0.15, while the right image shows the results when applying 0.17. By increasing the buffer slightly from 0.15 to 0.17, we aimed to detect as many shadows as possible. Additionally, since approximately 60% of Korea's land area is covered by forests, we redesigned the spectral threshold in the study by Zhong et al. [18] to consider regional and seasonal characteristics, as described by Equation (12). The method with the applied formula is illustrated in Figure 9. Finally, we assumed that one cloud object corresponds to one cloud shadow object. Figure 10a represents the state before noise removal, while (b) represents after noise removal. In PCS pixels, we extract an object with the largest outer contour, considering the rest as noise.

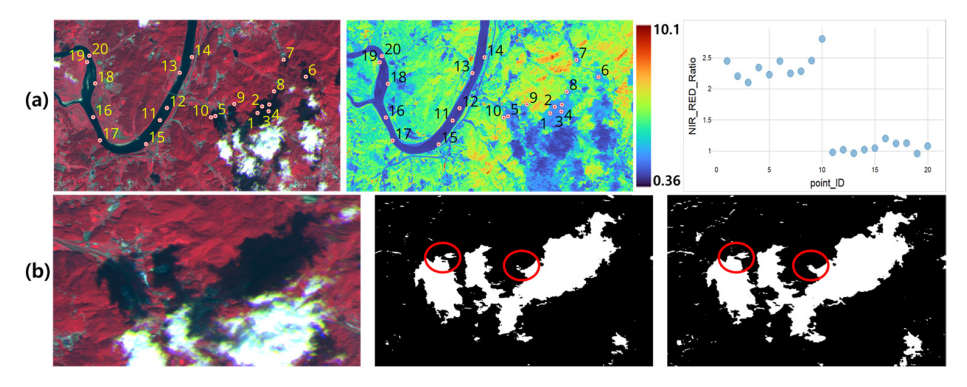


**Figure 8.** Examples for explanations of redesigning the spectral threshold by Equation (12): (a) explanation of the NIR-RED ratio values for shadows projected on vegetation and water; (b) reason for changing the NIR threshold.

Remote Sens. 2024, 16, 3950 9 of 22

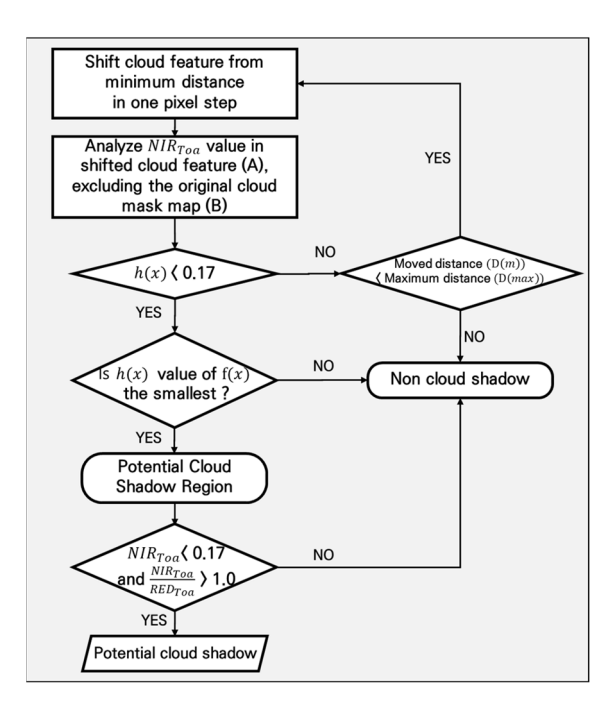


Figure 9. A decision tree diagram applied in Equations (9)–(12).

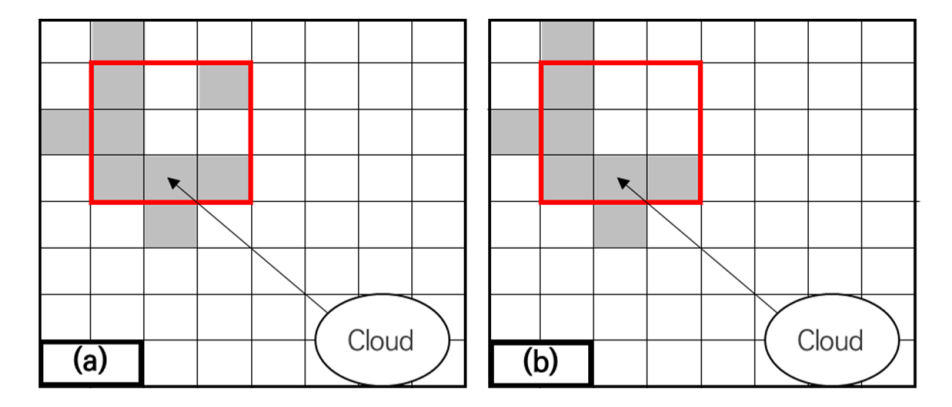


Figure 10. An example of noise removal: (a) before noise removal; (b) after noise removal.

## 3. Experiments

# 3.1. Datasets

In this study, cloud shadow detection experiments were conducted using RapidEye images at 5 m spatial resolution. As the images were provided at Level 1B, which is uncorrected for geometric distortion, geometric correction and orthorectification were applied based on the method developed in our previous studies [27–29]. To examine the impact of the relief displacement of clouds based on sensor geometry, we collected RapidEye images taken in similar regions and at similar times, focusing on viewing zenith angles ranging from near-nadir to oblique, with a maximum of 20 degrees. The solar azimuth and zenith angles were similar for each image acquisition. Figure 11 shows images used for the experiments. The left images in Figure 11 are represented as the NIR-R-G composite images, while the right images in Figure 11 are reference images where white pixels indicate clouds and black pixels represent cloud shadows. Table 1 summarizes the metadata of the images used in the experiments. All three images were taken in September over the Dongducheon-si and Gaesong-si, whose latitude difference is less than 0°7′35″ degrees. Therefore, the sun illumination angles for the three images were very similar.

Remote Sens. 2024, 16, 3950 10 of 22

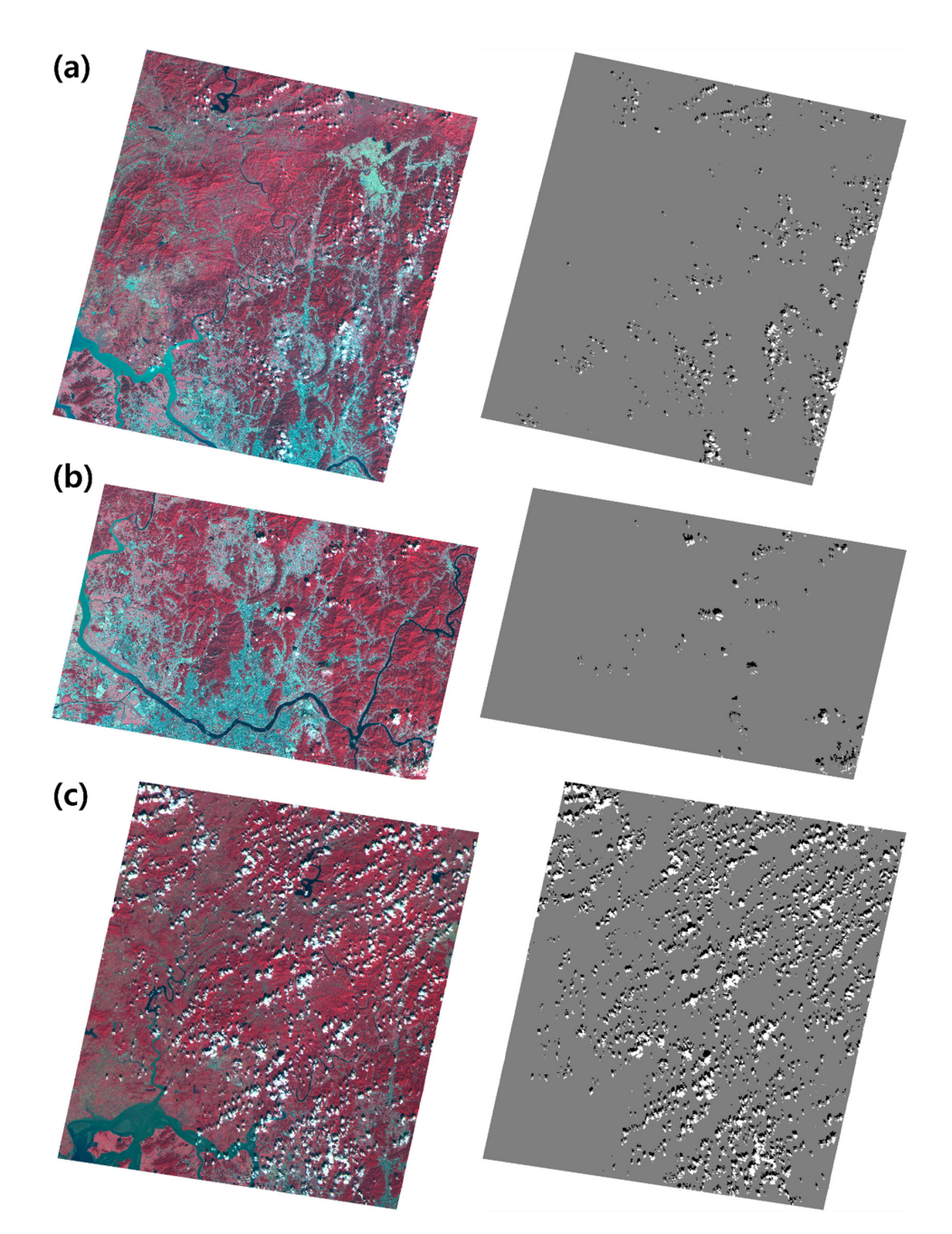


**Figure 11.** Satellite image and reference data used in the experiment: (a) Scene-1 image; (b) Scene-2 image; (c) Scene-3 image (white pixels and black pixels denote clouds and cloud shadows, respectively).

Image (a) was captured obliquely tilting the satellite to the west, with a sensor zenith angle of  $16.3^{\circ}$  and an azimuth angle of  $281.3^{\circ}$ . Image (b) was captured by near-vertically tilting the satellite to the east, with a sensor zenith angle of  $3.8^{\circ}$  and an azimuth angle of  $99.8^{\circ}$ . Image (c) was captured obliquely tilting the satellite to the east, with a sensor zenith angle of  $17.1^{\circ}$  and an azimuth angle of  $98.8^{\circ}$ . Note that the second image was captured with near-nadir viewing and that the other two images were captured with significant viewing angles in opposite directions to each other. Images (a)~(c) correspond to cloud cover percentages of 1.33%, 0.58%, and 12.66%, respectively. The cloud map was generated using the OCM method.

Remote Sens. 2024, 16, 3950 11 of 22

No. Category	Scene-1	Scene-2	Scene-3			
Acquisition date Cloud cover (%)	17 September 2018 1.33	27 September 2018 0.58	22 September 2018 12.66			
Sun's azimuth /zenith angle (°)	159.4/39.6	155.6/44.0	151.4/42.6			
Viewing azimuth /zenith angle (°)	281.3/16.3	99.8/3.8	98.8/17.1			
Used band	Red (555.0 nm), Near-infrared (710.0 nm)					
Product level	L1B					
Spatial resolution		5 m				

**Table 1.** Summary of information from RapidEye image used in experiment.

#### 3.2. Verification Method

To examine relief displacements of clouds in orthoimages, the direction of cloud shadows in orthoimages were estimated by first and second cases.

The cases were as follows:

- 1. The estimation of cloud shadows' direction angle based solely on sun illumination.
- 2. The estimation of cloud shadows' direction angle based on both sun illumination and sensor viewing direction.

The estimated direction of cloud shadows was compared with the true direction manually measured. We measured the true direction of the angles from a cloud to shadow through visual interpretation. Similarly, reference cloud shadow regions were extracted manually by visual interpretation using QGIS version 3.34.4.

#### 3.3. Performance Evaluation

The accuracy assessment involved qualitative and quantitative analyses by comparing the reference data with the results from the proposed method. A qualitative analysis was performed by visually interpreting the reference data. For a quantitative analysis, we used a confusion matrix that includes True Positive (TP), True Negative (TN), False Positive (FP), and False Negative (FN) metrics. These metrics are commonly employed in the field of detection to provide a quantitative evaluation of the proposed method. Furthermore, these metrics help to calculate the Precision, Recall, and F1 score. The Precision, Recall, and F1 score are derived from the confusion matrix results (Equations (13)–(15)) and represent the level of accuracy, with values closer to 1 indicating higher accuracy.

$$Precision = \frac{TP}{TP + FP'}$$
 (13)

$$Recall = \frac{TP}{TP + FN'}$$
 (14)

$$F1score = 2 \times \frac{Precision \times Recall}{Precision + Recall'}$$
 (15)

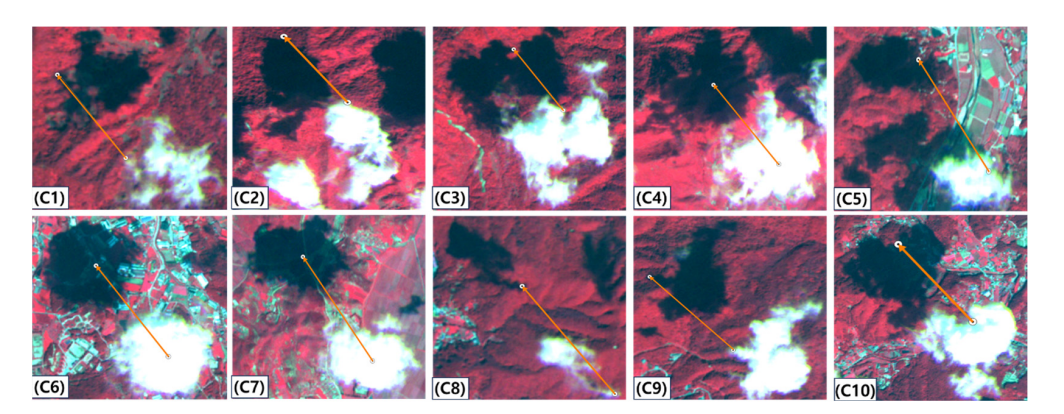
#### 4. Results

4.1. Verification of Cloud Shadow Direction: Comparing  $\overrightarrow{c_1}$  (Sun-Only Use) and  $\overrightarrow{c_2}$  (Sun and Sensor-Based Use) with True Directions

In this section, the verification of the direction angle for a cloud shadow was conducted. Verification data were collected by visually inspecting 10 direction angles from a cloud to shadow in each image. The collection criteria involved connecting the center of the cloud to the center of the cloud shadow or connecting the edge of the cloud to the corresponding edge of the cloud shadow, depending on the shape of the cloud and cloud shadows. Verification was performed by comparing the direction vector ( $\overrightarrow{C_1}$ ) of a cloud shadow obtained using

Remote Sens. 2024, 16, 3950 12 of 22

only the sun direction vector and the direction vector ( $\overrightarrow{C_2}$ ) obtained using both the solar direction vector and the sensor direction vector against the verification data ( $\overrightarrow{T}$ ).  $\overrightarrow{C_1}$  represents the first case mentioned in Section 3.2, where the distance is calculated using only the sun direction.  $\overrightarrow{C_2}$  represents the second case, where the distance is calculated considering both the sun and sensor directions. Figure 12 shows the 10 verification data values extracted from Scene-1, which was obtained by tilting the satellite to the west by 16.3°.



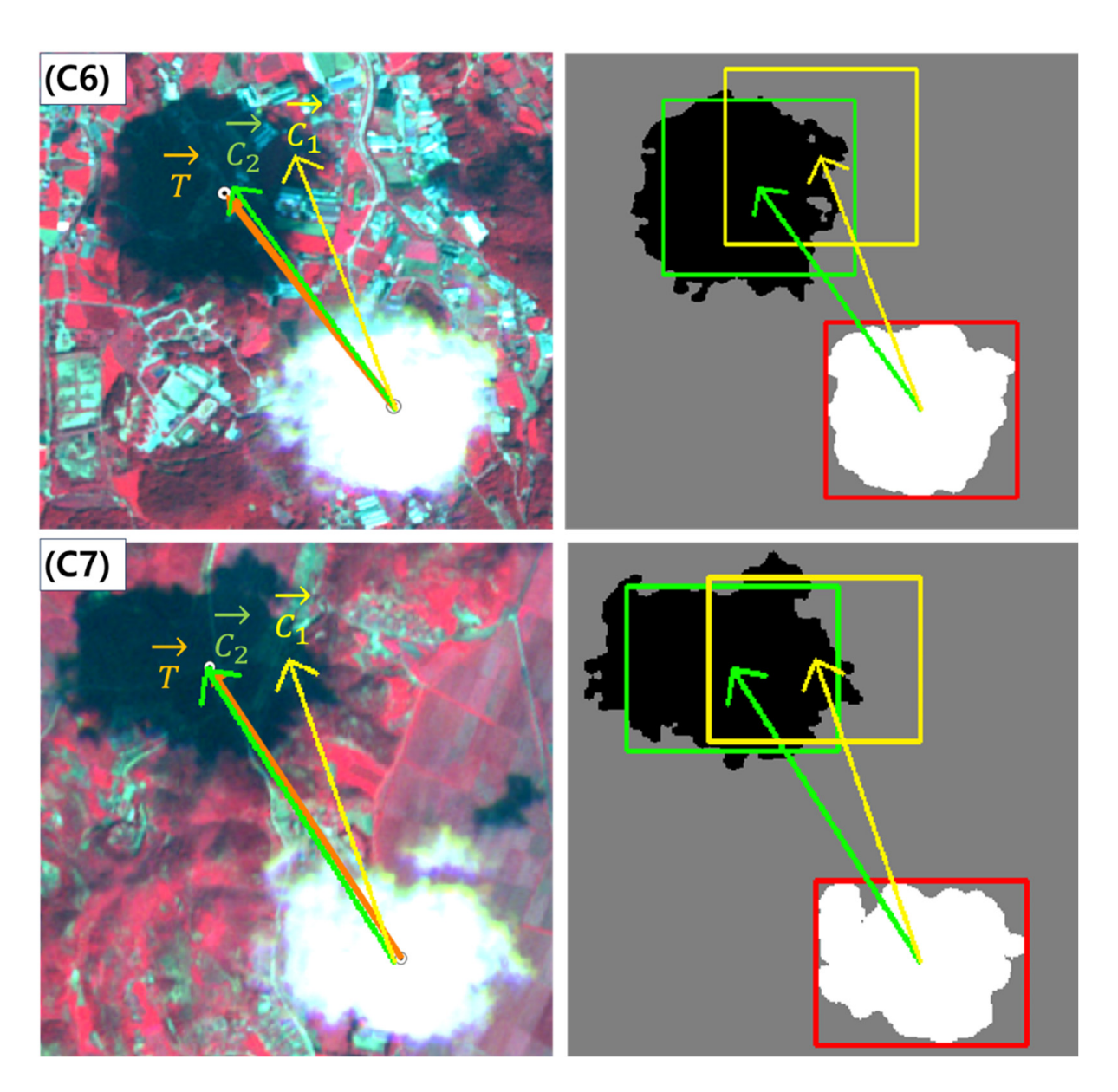
**Figure 12.** Verification data for checking azimuth angle of cloud shadow from cloud collected in Scene-1: (C1–C10) represent verification data 1 to 10 (C for case) from Scene-1 (the orange arrows represent  $\overrightarrow{T}$ ).

Figure 13 highlights the comparison of cloud shadow detection results for Scene-1. The left images represent the NIR-R-G composite images indicating the two direction angles of a cloud shadow,  $\overrightarrow{C_1}$ ,  $\overrightarrow{C_2}$ , and the verification data  $\overrightarrow{T}$ . The right image indicates the bounding boxes for a cloud shadow shifted from the bound box of clouds along the two cloud shadow directions. As shown in Figure 13,  $\overrightarrow{C_2}$  correctly points towards the center of the cloud shadow and the bounding box shifted along  $\overrightarrow{C_2}$  covers the entire cloud shadow region. Table 2 shows the angle values of  $\overrightarrow{C_1}$ ,  $\overrightarrow{C_2}$ , and  $\overrightarrow{T}$ ; the angle differences between  $\overrightarrow{C_1}$  and  $\overrightarrow{T}$ ; and the angle differences between  $\overrightarrow{C_2}$  and  $\overrightarrow{T}$  for 10 verification data values. The absolute mean angle difference between  $\overrightarrow{C_1}$  and  $\overrightarrow{T}$  was about 17.4° and that between  $\overrightarrow{C_2}$  and  $\overrightarrow{T}$  was about 3.2°. Figure 13 and Table 2 support the determination of cloud shadow directions using the sun and sensor directions, as proposed in this paper.

Table 2. A	Analysis resu	lts of the ver	ification data (	collected from	Scene-1.

Case	Angle Values for $\overset{ ightarrow}{C_1}$	Angle Values for $\overset{ ightarrow}{C_2}$	Angle Values for $\overset{ ightarrow}{T}$	$\overset{ ightarrow}{C_1} - \overset{ ightarrow}{T}$	$\overset{ ightarrow}{C_2} - \overset{ ightarrow}{T}$
Case 1		325.2°	322.8°	16.6°	2.4°
Case 2			324.4°	15.0°	0.8°
Case 3			323.8°	15.6°	1.4°
Case 4			321.3°	18.1°	3.9°
Case 5			321.8°	17.6°	3.4°
Case 6	339.4°		323.0°	16.4°	2.2°
Case 7			324.5°	14.9°	0.7°
Case 8			322.3°	17.1°	2.9°
Case 9			316.2°	23.2°	9.0°
Case 10			319.3°	20.1°	5.9°
Absolute Mean	-	-	-	17.4°	3.2°

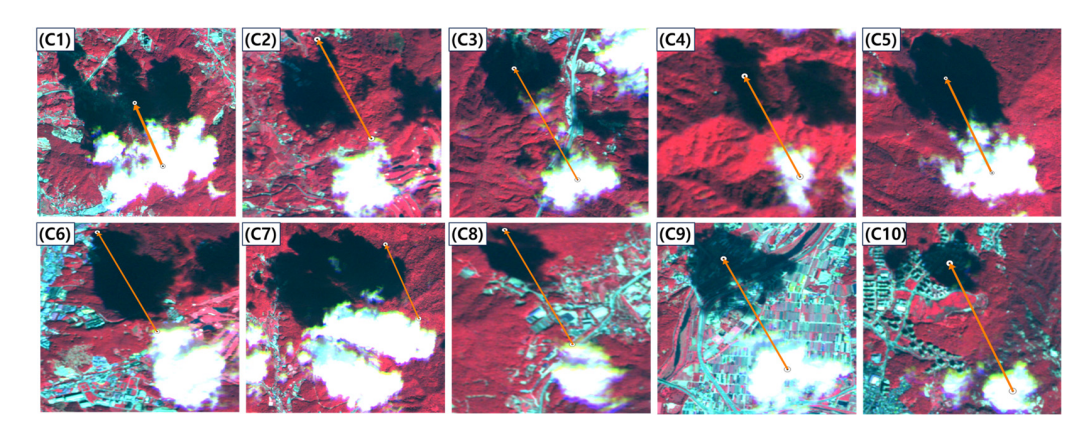
Remote Sens. **2024**, *16*, 3950



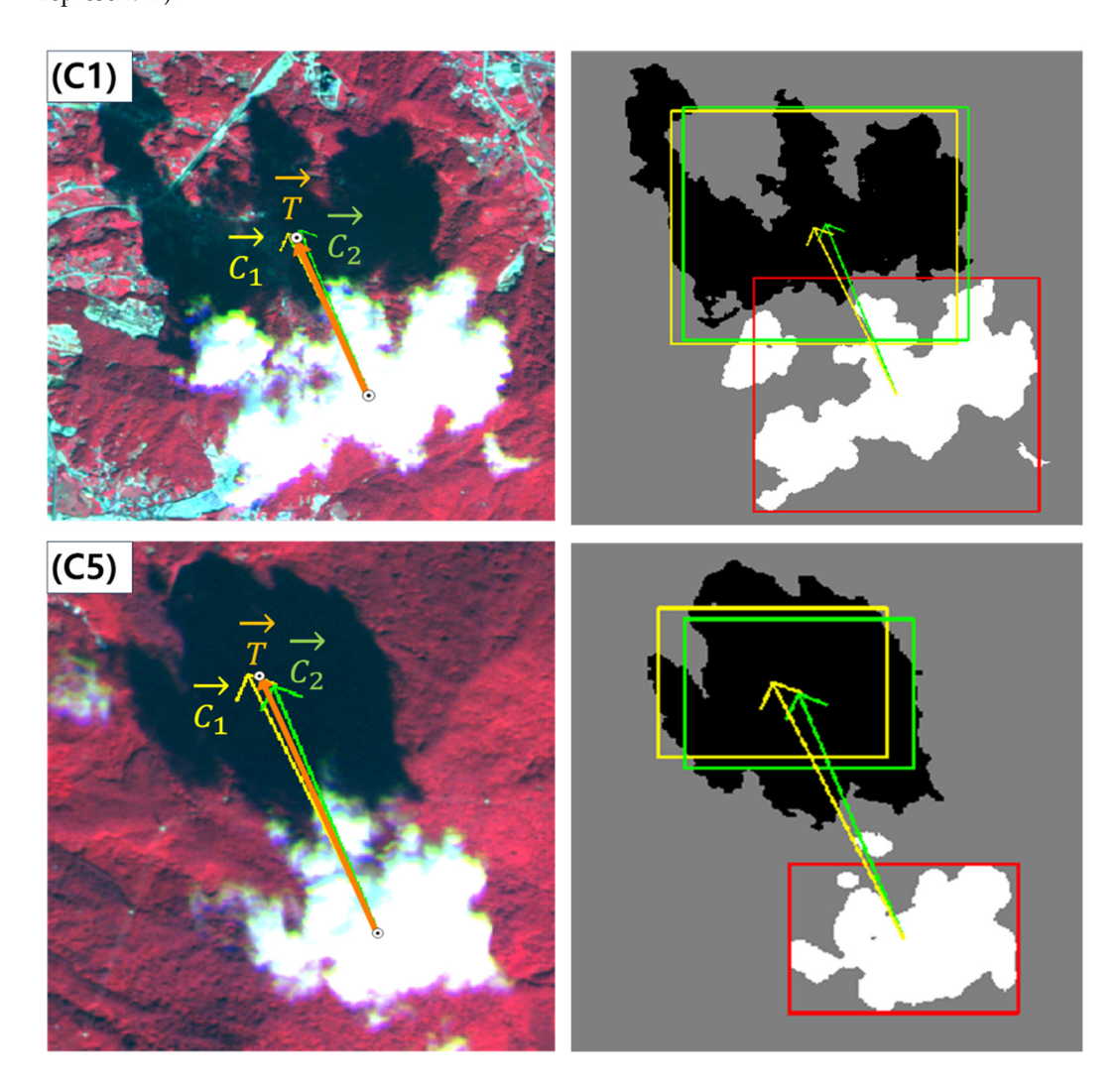
**Figure 13.** The result of comparing the yellow directional vector considering only the geometry of the sun and the green directional vector considering both a sensor and the sun geometry in Scene-1: **(C6)** a result of case 6 in Scene-1; **(C7)** a result of case 7 in Scene-1 (white pixels and black pixels denote clouds and cloud shadows, respectively).

Figure 14 shows the 10 verification data values extracted from Scene-2, which was obtained by a nearly vertical viewing angle. Figure 15 illustrates the comparison of cloud shadow detection results in Scene-2. For Scene-2, the differences between  $\overrightarrow{C_1}$  and  $\overrightarrow{C_2}$  were not as large as those in Scene-1. For near-vertical images, the relief displacements are not severe and hence the shadow direction angles using the sun direction are somewhat similar to those using the sun and sensor directions. As before, Table 3 shows the angle values of  $\overrightarrow{C_1}$ ,  $\overrightarrow{C_2}$ ,  $\overrightarrow{T}$ ,  $\overrightarrow{C_1}$  and  $\overrightarrow{T}$ , and  $\overrightarrow{C_2}$  and  $\overrightarrow{T}$  for Scene-2. The absolute mean angle difference between  $\overrightarrow{C_1}$  and  $\overrightarrow{T}$  was about 1.5° and that between  $\overrightarrow{C_2}$  and  $\overrightarrow{T}$  was about 2.3°. Figure 15 and Table 3 may indicate that sun directions can be used directly as cloud shadow directions for near-vertical images. They also support the proposed determination of cloud shadow directions using the sun and sensor directions for precise angle determination for near-vertical images.

Remote Sens. **2024**, 16, 3950



**Figure 14.** Verification data for checking azimuth angle of cloud shadow from cloud collected in Scene-2: (C1–C10) represent verification data 1 to 10 (C for case) from Scene-2 (the orange arrows represent  $\overset{\rightarrow}{T}$ ).



**Figure 15.** The result of comparing the yellow directional vector considering only the geometry of the sun and the green directional vector considering both a sensor and the sun geometry in Scene-2: **(C1)** a result of case 1 in Scene-2; **(C5)** a result of case 5 in Scene-2 (white pixels and black pixels denote clouds and cloud shadows, respectively).

Remote Sens. **2024**, 16, 3950 15 of 22

Case	Angle Values for $\overset{ ightarrow}{C_1}$	Angle Values for $\overset{ ightarrow}{C_2}$	Angle Values for $\overset{ ightarrow}{T}$	$\overset{ ightarrow}{C_1} - \overset{ ightarrow}{T}$	$\overset{ ightarrow}{C_2} - \overset{ ightarrow}{T}$
Case 1		339.1°	337.2°	-1.6	1.9
Case 2			336.5°	-0.9	2.6
Case 3			335.1°	0.5	4
Case 4			334.5°	1.1	4.6
Case 5	335.6°		337.9°	-2.3	1.2
Case 6			337.7°	-2.1	1.4
Case 7			337.8°	-2.1	1.3
Case 8			338.3°	-2.7	0.8
Case 9			335.1°	0.5	4
Case 10			337.3°	-1.7	1.8
Absolute Mean	-	-	-	1.5°	2.3°

**Table 3.** Analysis results of the verification data collected from Scene-2.

Figure 16 shows the 10 verification data values extracted from Scene-3, which was obtained by tilting to the east by 17.1°. Figure 17 illustrates the comparison of cloud shadow detection results in Scene-3. For Scene-3, the differences between  $\overrightarrow{C_1}$  and  $\overrightarrow{C_2}$  were as large as those in Scene-1. It is also notable that the location of shadow direction vectors,  $\overrightarrow{C_2}$ , and the corresponding shadow bounding boxes compared to the locations of  $\overrightarrow{C_1}$  and the corresponding shadow bounding boxes in Scene-3 are opposite to those in Scene-1. This is because Scene-3 was tilted to the east whereas Scene-1 was tilted to the west and hence relief displacements occurred in opposite directions. The proposed determination of cloud shadow directions could handle uncorrected cloud relief displacements in various tilt directions.

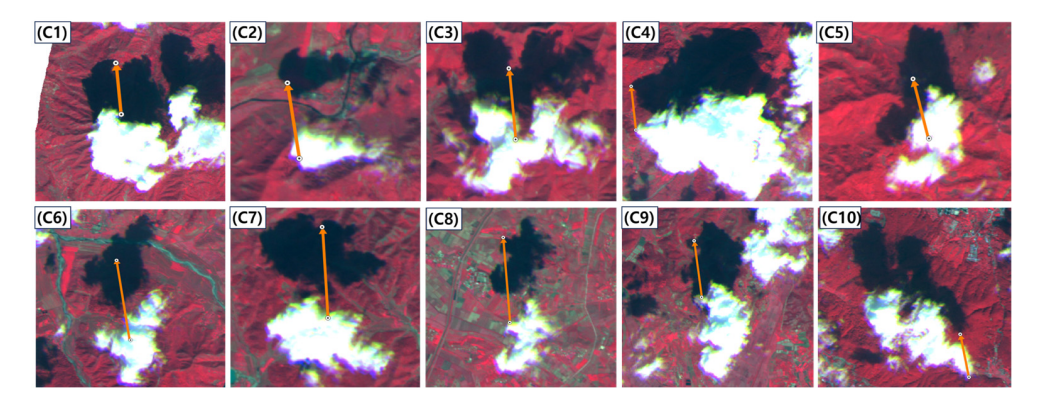


**Figure 16.** Verification data for checking azimuth angle of cloud shadow from cloud collected in Scene-3: (C1–C10) represent verification data 1 to 10 (C for case) from Scene-3 (the orange arrows represent  $\overset{\rightarrow}{T}$ ).

Table 4 shows the angle values of  $\overrightarrow{C_1}$ ,  $\overrightarrow{C_2}$ ,  $\overrightarrow{T}$ ,  $\overrightarrow{C_1}$  and  $\overrightarrow{T}$ , and  $\overrightarrow{C_2}$  and  $\overrightarrow{T}$  for Scene-3. The absolute mean angle difference between  $\overrightarrow{C_1}$  and  $\overrightarrow{T}$  was about 21.3° and that between  $\overrightarrow{C_2}$  and  $\overrightarrow{T}$  was about 3.7°. The magnitude of the absolute mean angle difference between  $\overrightarrow{C_1}$  and  $\overrightarrow{T}$  for Scene-3 was larger than that for Scene-1. This is because the magnitude of the sensor's tilt angle for Scene-3 was larger than for Scene-1. The results and observations in Figure 17 and Table 4 strongly support that the proposed determination of cloud shadow directions using the sun and sensor directions should be valid.

Remote Sens. **2024**, 16, 3950

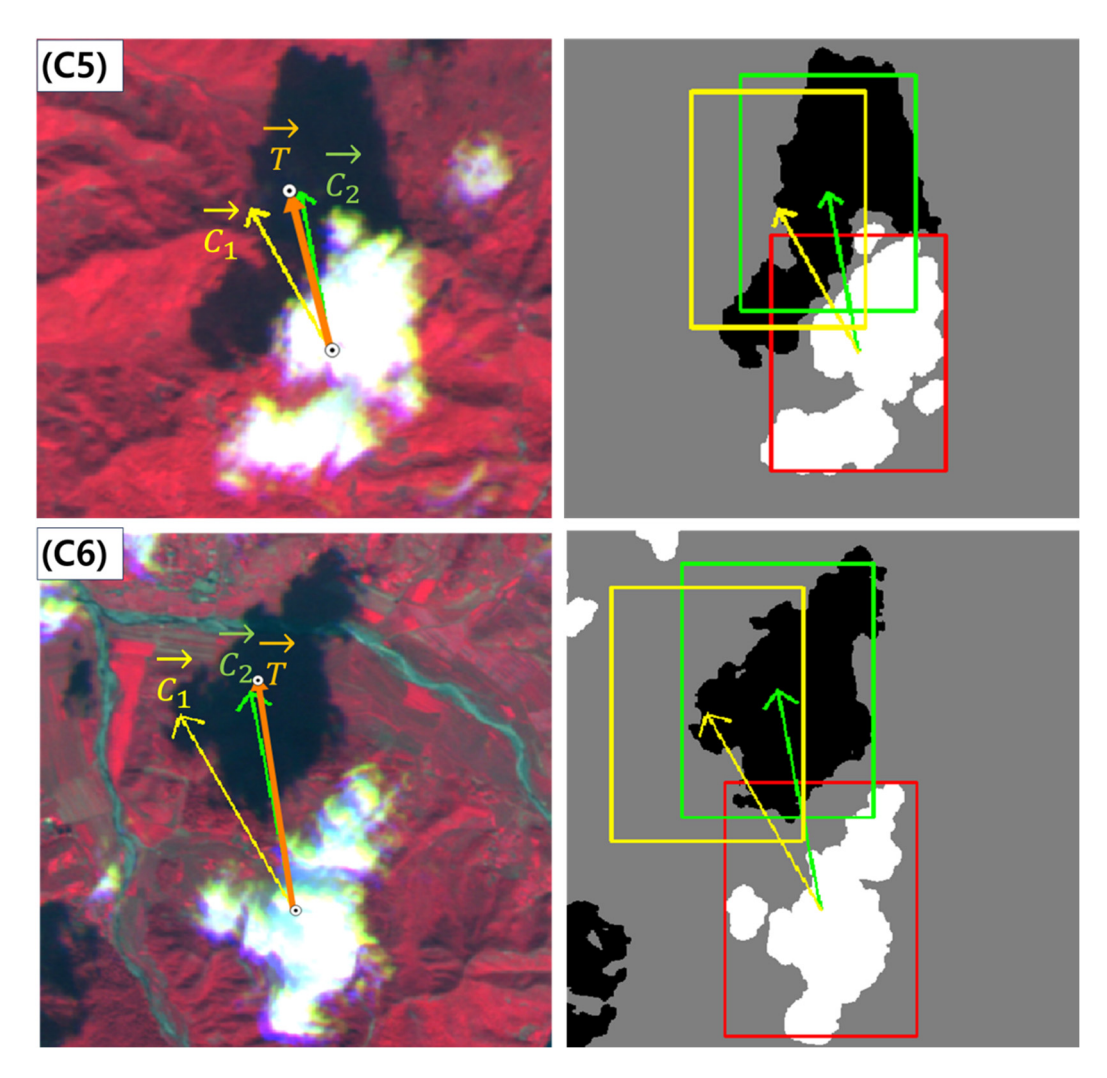


**Figure 17.** The result of comparing the yellow directional vector considering only the geometry of the sun and the green directional vector considering both a sensor and the sun geometry in Scene-3: **(C5)** a result of case 5 in Scene-3; **(C6)** a result of case 6 in Scene-3 (white pixels and black pixels denote clouds and cloud shadows, respectively).

**Table 4.** Analysis results of the verification data collected from Scene-3.

Case	Angle Values for $\overset{ ightarrow}{C_1}$	Angle Values for $\overset{ ightarrow}{C_2}$	Angle Values for $\overset{ ightarrow}{T}$	$\overset{ ightarrow}{C_1}-\overset{ ightarrow}{T}$	$\overset{ ightarrow}{C_2} - \overset{ ightarrow}{T}$
Case 1		349.8°	355.1°	-23.8°	−5.3°
Case 2			351.8°	−20.5°	-2.0°
Case 3			354.0°	-22.7°	-4.2°
Case 4	- - - - -		354.1°	-22.8°	-4.3°
Case 5			346.0°	-14.7°	3.8°
Case 6			351.4°	-20.1°	-1.6°
Case 7			$-25.4^{\circ}$	-25.4°	-6.9°
Case 8			355.6°	-24.3°	−5.8°
Case 9			352.4°	-21.1°	-2.6°
Case 10			349.3°	−18.0°	0.5°
Absolute Mean	-	-	-	21.3°	3.7°

Remote Sens. 2024, 16, 3950 17 of 22

# 4.2. Comparative Analysis of $\overrightarrow{c_1}$ and $\overrightarrow{c_2}$ in Proposed Method

In this section, we conducted an accuracy analysis of cloud shadow detection results using  $\overrightarrow{C_1}$  and  $\overrightarrow{C_2}$ . Figure 18 shows the intermediate process of cloud shadow detection using  $\overrightarrow{C_1}$  and  $\overrightarrow{C_2}$  for Scene-3. In Figure 18, (a) represents the NIR-R-G composite image. (b) to (e) illustrate the location of a shifted cloud object using  $\overrightarrow{C_1}$  and h(x) as described by Equation (10), while (f) to (i) illustrate the same for  $\overrightarrow{C_2}$ . The NIR located in the top right corner of the figure represents the statistics as described in Equation (9), which are equivalent to h(x). Orange pixels represent a shifted cloud object, while red pixels indicate PCSR as described in Equation (11). Yellow directional vectors represent  $\overrightarrow{C_1}$ , and green directional vectors represent  $\overrightarrow{C_2}$ .

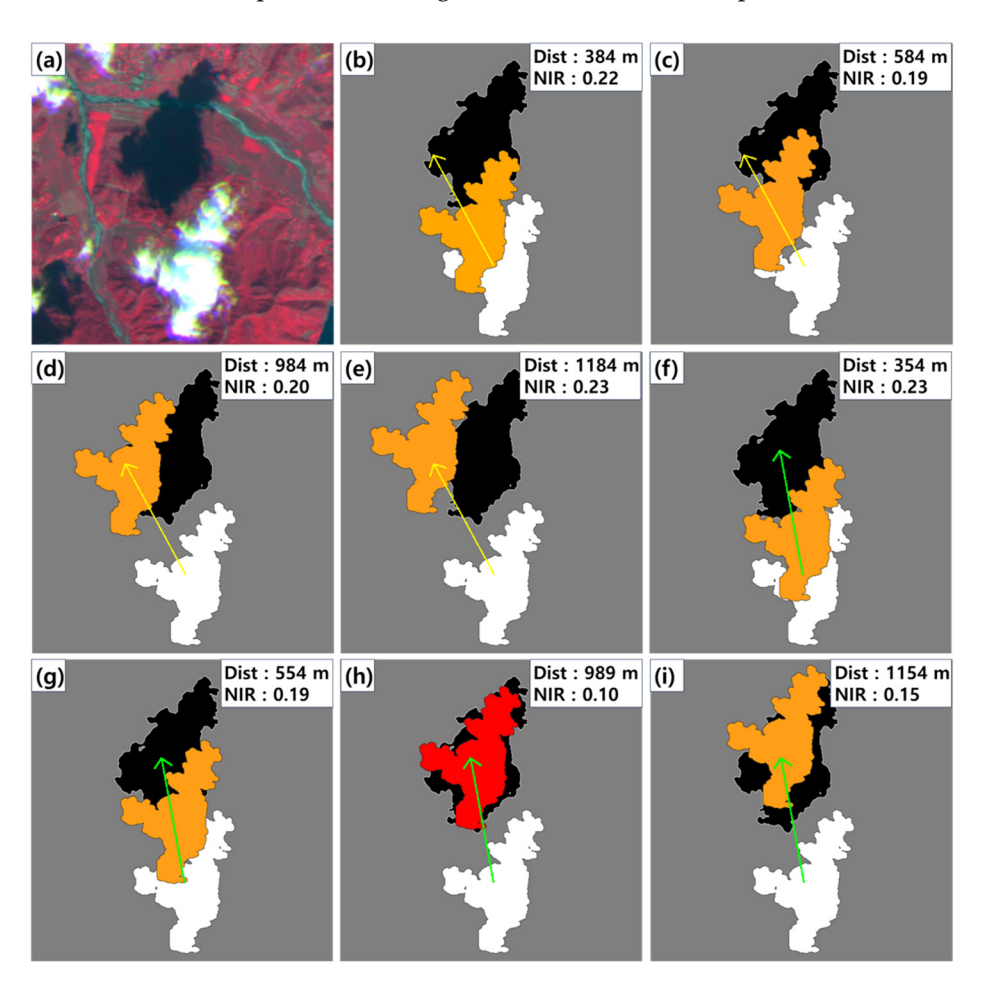


**Figure 18.** Intermediate process of cloud shadow detection for searching PCSR in Scene-3: (a) the NIR-R-G composite image; (b-e) the process of shadow detection based on distance using  $\overrightarrow{C_1}$ ; (f-i) that using  $\overrightarrow{C_2}$  (white pixels and black pixels denote clouds and cloud shadows, respectively).

The distance for cloud shadow detection in C6 of Scene-3 was confirmed to be 989 m as seen in (h) using  $\overrightarrow{C_2}$ . However, it was observed that when using  $\overrightarrow{C_1}$ , the corresponding cloud shadow was not detected at distances like those of  $\overrightarrow{C_2}$ , and was skipped. For the same reasons mentioned in Section 4.1, a precise cloud shadow directional angle was not set. These results further support the validity of cloud shadow direction determination using the direction of the sun and sensor in the orthoimage. Despite having validated this method, it may still exhibit a potential sensitivity under certain conditions, such as varying spectral characteristics of the imagery, including spectral conditions relevant to cloud shadow detection, or variations in the azimuth and zenith angles of the sun and

Remote Sens. 2024, 16, 3950 18 of 22

sensor. A more detailed discussion of these limitations and potential improvements is provided in the Discussion and Conclusions Section.

Figure 19 illustrates the post-processing process following the detection of PCSR. Figure 19a represents the reference data for clouds and cloud shadows, while (b) denotes before post-processing, and (c) post-processing. The red pixels in (b) and (c) represent final cloud shadow pixels, while yellow pixels denote remaining noise pixels such as terrain shadows or water bodies. PCS was detected within the boundary of the shifted cloud using Equation (11), such as in C6 of Figure 17, which is indicated by the green bounding box. Subsequently, the PCS of the object with the largest outer contour of the detected pixels, as shown in Figure 19c, is considered the final cloud shadow.

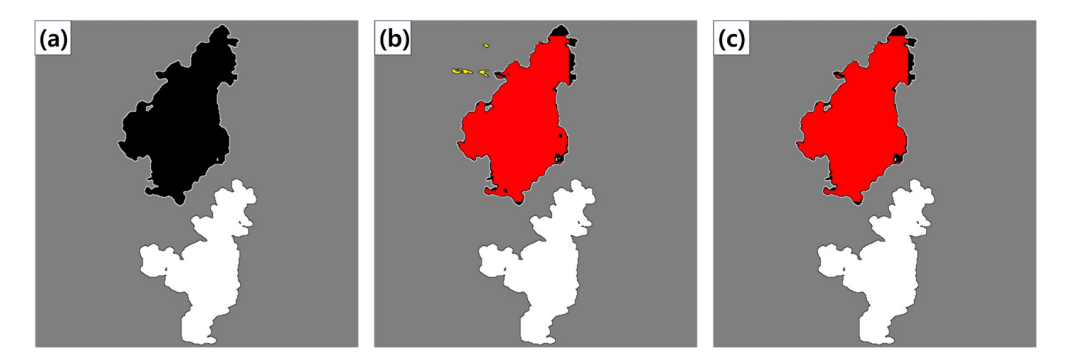


**Figure 19.** Post-processing process for cloud shadow detection: (a) the reference data; (b) cloud shadow detection before post-processing; (c) cloud shadow detection after post-processing(white pixels and black pixels denote clouds and cloud shadows, respectively).

# 4.3. Evaluation of Cloud Shadow Detection Accuracy with $\overrightarrow{c_1}$ and $\overrightarrow{c_2}$ in Proposed Method

The results of cloud shadow detection are presented in Figures 20–22 for Scene-1, -2, and -3, respectively. In these figures, (a) to (c) represent, in order, the reference cloud and cloud shadows, the detection results using  $\overrightarrow{C_1}$ , and the detection results using  $\overrightarrow{C_2}$ . White pixels represent clouds detected separately by the OCM method [18] and black pixels represent cloud shadows. One can observe that the shadow detection results using  $\overrightarrow{C_1}$  could not find cloud shadows at all, in particular for Scene-1 and Scene-3. This is because the wrong cloud shadow directions could not guide the shifted cloud shadow bounding boxes to the location close enough to the real cloud shadow.

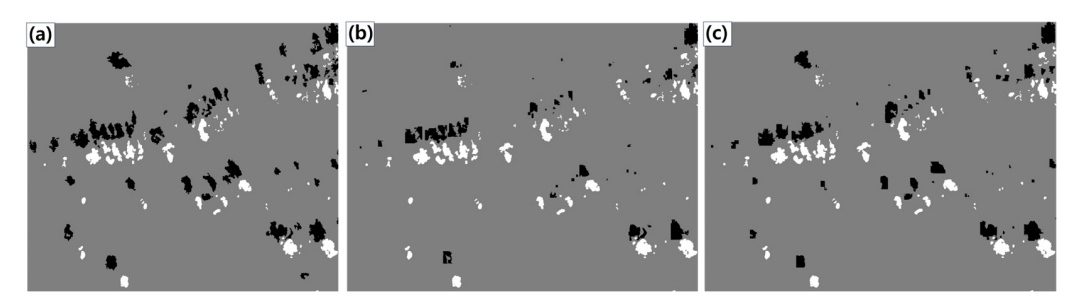


**Figure 20.** Cloud shadow detection results from Scene-1 images (white pixels and black pixels denote clouds and cloud shadows, respectively):  $(\mathbf{a}-\mathbf{c})$  represent, in sequence, the reference cloud and cloud shadows, the detection results using  $\overset{\rightarrow}{C_1}$ , and the detection results using  $\overset{\rightarrow}{C_2}$  from an enlarged image.

Remote Sens. 2024, 16, 3950 19 of 22

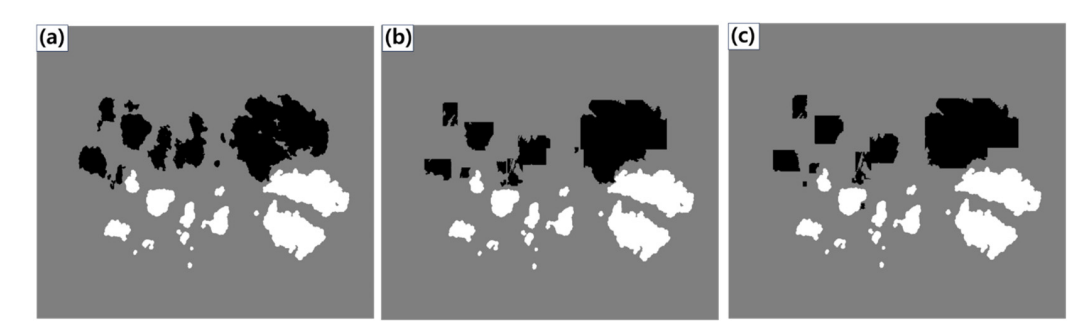


**Figure 21.** Cloud shadow detection results from Scene-2 images (white pixels and black pixels denote clouds and cloud shadows, respectively): (**a–c**) represent, in sequence, the reference cloud and cloud shadows, the detection results using  $\overrightarrow{C_1}$ , and the detection results using  $\overrightarrow{C_2}$  from an enlarged image.

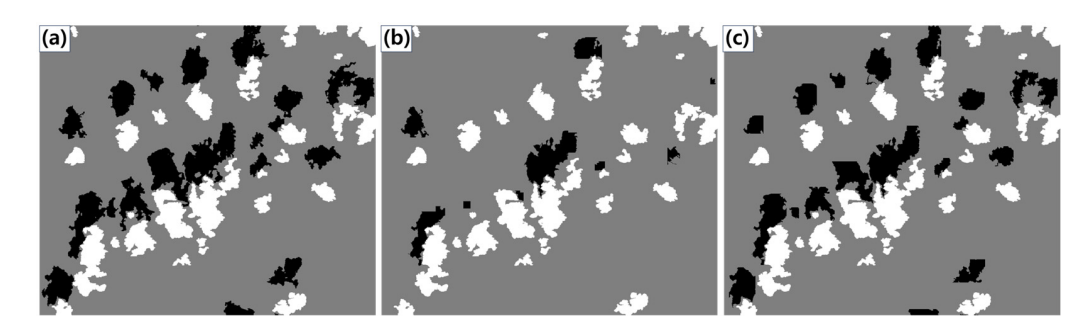


**Figure 22.** Cloud shadow detection results from Scene-3 images (white pixels and black pixels denote clouds and cloud shadows, respectively): (**a–c**) represent, in sequence, the reference cloud and cloud shadows, the detection results using  $\overset{\rightarrow}{C_1}$ , and the detection results using  $\overset{\rightarrow}{C_2}$  from an enlarged image.

On the other hand, the cloud shadow detection using  $\overrightarrow{C_2}$  successfully identified the cloud shadows corresponding to the clouds, but there was a small shape discrepancy in some results compared to reference data. This discrepancy could be attributed to the variation in the shadow's shape caused by the terrain relief.

Quantitative analysis results for the three scenes using  $\overrightarrow{C_1}$  and  $\overrightarrow{C_2}$  are summarized in Table 5. They indicate that the metrics values are consistently higher when using  $\overrightarrow{C_2}$  for Scene-1 and -3. In the case of Scene-1, the detection rate was 97.5% for  $\overrightarrow{C_2}$ , while it was 86.2% for  $\overrightarrow{C_1}$ . In the case of Scene-3, the detection rate for  $\overrightarrow{C_2}$  was 94.0%, while it was 80.8% for  $\overrightarrow{C_1}$ . For Scene-2, the shadow detection results from  $\overrightarrow{C_1}$  and  $\overrightarrow{C_2}$  were very similar to each other. This is because  $\overrightarrow{C_1}$  and  $\overrightarrow{C_2}$  were very similar and the locations of shifted bounding boxes were also very similar.

 Table 5. Accuracy result of cloud shadow detection according to two vectors in experiment images.

No		Accuracy of Cloud Shadow Detection in Scene-1 Using		Accuracy of Cloud Shadow Detection in Scene-2 Using		Accuracy of Cloud Shadow Detection in Scene-3 Using	
	$\overset{ ightarrow}{C_1}$	$\overset{ ightarrow}{C_2}$	$\overset{ ightarrow}{C_1}$	$\overset{ ightarrow}{C_2}$	$\overset{ ightarrow}{C_1}$	$\overset{ ightarrow}{C_2}$	
Precision	0.79	0.87	0.80	0.82	0.93	0.96	
Recall	0.32	0.59	0.45	0.45	0.33	0.62	
F1 score	0.46	0.70	0.58	0.58	0.49	0.76	
Detection ratio (%)	86.2	97.5	99.6	98.3	80.8	94.0	
Total cloud objects	1332		30	300		2011	

Bold text represents better or equal performance.

Remote Sens. 2024, 16, 3950 20 of 22

The average F1 scores for cases using  $\overrightarrow{C_1}$  and  $\overrightarrow{C_2}$  are 0.51 and 0.68, respectively. The detection accuracy of  $\overrightarrow{C_2}$  improved by 0.17 compared to  $\overrightarrow{C_1}$ . The average detection rates for  $\overrightarrow{C_1}$  and  $\overrightarrow{C_2}$  are calculated as 88.8% and 96.5%, respectively. This result confirms that, even if the relief displacement of clouds is not corrected in the orthoimages, the proposed method allows for more accurate cloud shadow detection.

#### 5. Discussion and Conclusions

This study has demonstrated that in orthoimages, both the direction of sun illumination and the sensor viewing direction should be considered to determine the precise direction of a cloud shadow. This is because the relief displacements of the cloud are not corrected through orthorectification processes. To verify this, we conducted experiments using orthoimages generated from both near-nadir and oblique viewing angles.

Results in Section 4.1, Verification of Cloud Shadow Direction, showed that the direction of cloud shadows determined by both the sun illumination and sensor viewing directions  $(C_2)$  was more precise, with a maximum deviation of 3.7° from the true direction  $(\overrightarrow{T})$ , compared to the maximum deviation of 21.3° when using only the sun illumination  $(C_1)$ . In the Scene-2 image captured with near-nadir viewing,  $C_2$  showed slightly lower performance compared to high-oblique images. The results indicated that the sensor viewing angles are sensitive to performance in images captured with near-nadir viewing. This indicates that the geometric relationship between viewing angles warrants further investigation, and a more comprehensive analysis of performance across a broader range of azimuth and zenith angles would be a valuable extension of this research. Results in Section 4.3, concerning cloud shadow detection accuracy, showed that the shadow detection considering the angle from the second case ( $C_2$ ) improved the average F1 score by 0.17 and increased the average detection rate by 7.7%, compared to the results from the first case  $(C_1)$ . By considering both solar and sensor geometries, higher accuracy in cloud shadow detection was achieved. This result supports the estimation of shadow direction from clouds with uncorrected relief displacements and cloud shadow detection proposed in this paper. While this study focused on a dataset composed of relatively small cumulus clouds, and this algorithm may face challenges in maintaining the same level of accuracy under more diverse conditions, such as larger cloud structures or in varying seasonal environments, further research would be valuable to explore how well the method generalizes to other cloud types and seasonal characteristics.

Nevertheless, these findings lay a solid foundation for further refinement and application in more complex scenarios. The inclusion of sensor geometry improved the accuracy of the estimation of cloud shadow directions. This improvement contributed to significant improvements for detecting cloud shadows. By shifting a bounding box of a cloud region through the cloud shadow direction, we could locate the bounding box on cloud shadows. Cloud shadow regions were extracted precisely by identifying dark pixels within the box. The findings in this paper should apply to detecting cloud shadows in high-resolution satellite orthoimages. Additionally, these findings have the potential to be expanded for the shadow detection of other objects with uncorrected relief displacements, such as high-rise buildings in UAV images. This can be a new and interesting research topic.

In future research, we plan to extend this study by exploring the generalization of our method to different cloud types and more diverse seasonal conditions. Additionally, we aim to further investigate the geometric relationship between solar and sensor viewing angles to enhance cloud shadow detection under various viewing geometries. Finally, we will explore the potential applications of this method to detect shadows from other objects with uncorrected relief displacements, such as high-rise buildings in UAV images.

Remote Sens. 2024, 16, 3950 21 of 22

**Author Contributions:** Conceptualization, T.K. and H.K.; methodology, H.K.; validation, T.K. and W.Y.; investigation, H.K.; writing—original draft preparation, H.K.; writing—review and editing, T.K., H.K., and W.Y.; visualization, W.Y.; supervision, T.K.; project administration, T.K.; funding acquisition, T.K. All authors have read and agreed to the published version of the manuscript.

**Funding:** This study was supported jointly by the Korea Forest Service's Nation Institute of Forest Science under the project titled "Reception, Processing, ARD Standardization, and Development of Intelligent Forest Information Platform (task number: FM0103-2021-01) and by the Korea Agency for Infrastructure Technology Advancement grant funded by the Ministry of Land, Infrastructure and Transport (RS-2022-00141819, Development of Advanced Technology for Absolute, Relative, and Continuous Complex Positioning to Acquire Ultra-precise Digital Land Information).

**Data Availability Statement:** The original contributions presented in the study are included in the article; further inquiries can be directed to the corresponding author.

Conflicts of Interest: The authors declare no conflicts of interest.

#### References

- 1. Kang, J.; Kim, G.; Jeong, Y.; Kim, S.; Youn, Y.; Cho, S.; Lee, Y. U-Net Cloud Detection for the SPARCS Cloud Dataset from Landsat 8 Images. *Korean J. Remote Sens.* **2021**, 37, 1149–1161. [CrossRef]
- 2. Shahtahmassebi, A.; Yang, N.; Wang, K.; Moore, N.; Shen, Z. Review of shadow detection and de-shadowing methods in remote sensing. *Chin. Geogr. Sci.* 2013, 23, 403–420. [CrossRef]
- 3. Mostafa, Y. A review on various shadow detection and compensation techniques in remote sensing images. *Can. J. Remote Sens.* **2017**, *43*, 545–562. [CrossRef]
- 4. Aboutalebi, M.; Torres-Rua, A.F.; Kustas, W.P.; Nieto, H.; Coopmans, C.; McKee, M. Assessment of different methods for shadow detection in high-resolution optical imagery and evaluation of shadow impact on calculation of NDVI, and evapotranspiration. *Irrig. Sci.* 2019, 37, 407–429. [CrossRef]
- 5. Liu, X.; Yang, F.; Wei, H.; Gao, M. Shadow Removal from UAV Images Based on Color and Texture Equalization Compensation of Local Homogeneous Regions. *Remote Sens.* **2022**, *14*, 2616. [CrossRef]
- 6. Alavipanah, S.K.; Karimi Firozjaei, M.; Sedighi, A.; Fathololoumi, S.; Zare Naghadehi, S.; Saleh, S.; Naghdizadegan, M.; Gomeh, Z.; Arsanjani, J.J.; Makki, M.; et al. The Shadow Effect on Surface Biophysical Variables Derived from Remote Sensing: A Review. *Land* 2022, 11, 2025. [CrossRef]
- 7. Mao, K.B.; Yuan, Z.J.; Zuo, Z.Y.; Xu, T.R.; Shen, X.Y.; Gao, C.Y. Changes in global cloud cover based on remote sensing data from 2003 to 2012. *Chin. Geogr. Sci.* **2019**, *29*, 306–315. [CrossRef]
- 8. Kim, B.H.; Kim, Y.; Han, Y.K.; Choi, W.S.; Kim, Y. Fully Automated Generation of Cloud-free Imagery Using Landsat-8. *J. Korean Soc. Surv. Geod. Photogramm. Cartogr.* **2014**, *32*, 133–142. [CrossRef]
- 9. Byeon, Y.; Choi, S.; Jin, D.; Seong, N.; Jung, D.; Sim, S.; Woo, J.; Jeon, U.; Han, K. Quality Evaluation through Inter-Comparison of Satellite Cloud Detection Products in East Asia. *Korean J. Remote Sens.* **2021**, *37*, 1829–1836. [CrossRef]
- 10. Zekoll, V.; de los Reyes, R.; Richter, R. A Newly Developed Algorithm for Cloud Shadow Detection—TIP Method. *Remote Sens.* **2022**, *14*, 2922. [CrossRef]
- 11. Li, Z.; Shen, H.; Li, H.; Xia, G.; Gamba, P.; Zhang, L. Multi-feature combined cloud and cloud shadow detection in GaoFen-1 wide field of view imagery. *Remote Sens. Environ.* **2017**, 191, 342–358. [CrossRef]
- 12. Zhang, C.; Weng, L.; Ding, L.; Xia, M.; Lin, H. CRSNet: Cloud and Cloud Shadow Refinement Segmentation Networks for Remote Sensing Imagery. *Remote Sens.* **2023**, *15*, 1664. [CrossRef]
- 13. Tan, Y.; Zhang, W.; Yang, X.; Liu, Q.; Mi, X.; Li, J.; Yang, J.; Gu, X. Cloud and Cloud Shadow Detection of GF-1 Images Based on the Swin-UNet Method. *Atmosphere* **2023**, *14*, 1669. [CrossRef]
- 14. Zhu, Z.; Wang, S.; Woodcock, C.E. Improvement and expansion of the Fmask algorithm: Cloud, cloud shadow, and snow detection for Landsats 4–7, 8, and Sentinel 2 images. *Remote Sens. Environ.* **2015**, 159, 269–277. [CrossRef]
- 15. Foga, S.; Scaramuzza, P.L.; Guo, S.; Zhu, Z.; Dilley, R.D.; Beckmann, T.; Schmidt, G.L.; Dwyer, J.L.; Joseph Hughes, M.; Laue, B. Cloud Detection Algorithm Comparison and Validation for Operational Landsat Data Products. *Remote Sens. Environ.* **2017**, 194, 379–390. [CrossRef]
- 16. Le Hegarat-Mascle, S.; Andre, C. Use of Markov Random Fields for automatic cloud/shadow detection on high resolution optical images. *ISPRS J. Photogramm. Remote Sens.* **2009**, *64*, 351–366. [CrossRef]
- 17. Fisher, A. Cloud and Cloud-Shadow Detection in SPOT5 HRG Imagery with Automated Morphological Feature Extraction. *Remote Sens.* **2014**, *6*, 776–800. [CrossRef]
- 18. Zhong, B.; Chen, W.; Wu, S.; Hu, L.; Luo, X.; Liu, Q. A cloud detection method based on relationship between objects of cloud and cloud-shadow for Chinese moderate to high resolution satellite imagery. *IEEE J. Sel. Top. Appl. Earth Obs. Remote Sens.* **2017**, 10, 4898–4908. [CrossRef]
- 19. Pailot-Bonnétat, S.; Harris, A.J.L.; Calvari, S.; De Michele, M.; Gurioli, L. Plume Height Time-Series Retrieval Using Shadow in Single Spatial Resolution Satellite Images. *Remote Sens.* **2020**, *12*, 3951. [CrossRef]

Remote Sens. 2024, 16, 3950 22 of 22

20. Prabhakar, M.; Gopinath, K.; Reddy, A.; Thirupathi, M.; Rao, C.S. Mapping hailstorm damaged crop area using multispectral satellite data. *Egypt. J. Remote Sens. Space Sci.* **2019**, 22, 73–79. [CrossRef]

- 21. Elsharkawy, A.; Elhabiby, M.; El-Sheimy, N. New combined pixel/object-based technique for efficient urban classification using WorldView-2 data. *Int. Arch. Photogramm. Remote Sens. Spat. Inf. Sci.* **2012**, *39*, 191–195. [CrossRef]
- 22. Satellite Imagery Product Specifications. Available online: https://assets.planet.com/docs/1601.RapidEye.Image.Product.Specs\_ Jan16\_V6.1\_ENG.pdf (accessed on 10 January 2024).
- 23. Luo, Y.; Trishchenko, A.P.; Khlopenkov, K.V. Developing Clear-Sky, Cloud and Cloud Shadow Mask for Producing Clear-Sky Composites at 250-Meter Spatial Resolution for the Seven MODIS Land Bands over Canada and North America. *Remote Sens. Environ.* 2008, 112, 4167–4185. [CrossRef]
- 24. Sun, L.; Liu, X.; Yang, Y.; Chen, T.T.; Wang, Q.; Zhou, X. A Cloud Shadow Detection Method Combined with Cloud Height Iteration and Spectral Analysis for Landsat 8 OLI Data. *ISPRS J. Photogramm. Remote Sens.* **2018**, *138*, 193–207. [CrossRef]
- 25. Leblon, B.; Gallant, L.; Granberg, H. Effects of Shadowing Types on Ground-Measured Visible and Near-Infrared Shadow Reflectances. *Remote Sens. Environ.* **1996**, *58*, 322–328. [CrossRef]
- 26. Kustiyo; Dianovita, H.; Ismaya, H.; Rahayu, M.I.; Adiningsih, E.S. New Automated Cloud and Cloud-Shadow Detection Using Landsat Imagery. *Int. J. Remote Sens. Earth Sci.* **2012**, *9*, 100–111. [CrossRef]
- 27. Yoon, W. A Study on Development of Automatic GCP Matching Technology for CAS-500 Imagery. Master's Thesis, Inha University, Incheon, Republic of Korea, 2019.
- 28. Park, H.; Son, J.H.; Jung, H.S.; Kweon, K.E.; Lee, K.D.; Kim, T. Development of the Precision Image Processing System for CAS-500. *Korean J. Remote Sens.* **2020**, *36*, 881–891. [CrossRef]
- 29. Son, J.H.; Yoon, W.; Kim, T.; Rhee, S. Iterative Precision Geometric Correction for High-Resolution Satellite Images. *Korean J. Remote Sens.* **2021**, 37, 431–447. [CrossRef]

**Disclaimer/Publisher's Note:** The statements, opinions and data contained in all publications are solely those of the individual author(s) and contributor(s) and not of MDPI and/or the editor(s). MDPI and/or the editor(s) disclaim responsibility for any injury to people or property resulting from any ideas, methods, instructions or products referred to in the content.